Dynamical Forecasting and Dynamical Interpolation: An Experiment in the California Current

ALLAN R. ROBINSON, JAMES A. CARTON AND NADIA PINARDI

Center for Earth and Planetary Physics, Harvard University, Cambridge, MA 02138

CHRISTOPHER N. K. MOOERS

Department of Oceanography, Naval Postgraduate School, Monterey, CA 93943

(Manuscript received 20 August 1985, in final form 10 February 1986)

ABSTRACT

In order to perform real-time dynamical forecasts and hindcasts, three high-resolution hydrographic surveys were made of a (150 km)^2 domain off northern California, providing two sets of initialization and verification fields. The data was objectively analyzed and regularly gridded for model compatibility. These maps initially show an anticyclonic eddy segment in the northeast and part of another in the northwest. Two weeks later only the northwest anticyclonic eddy remained, with the domain center dominated by a 0.6 m s^{-1} jet. Two weeks after that only a larger northwest eddy with fairly weak velocities remained. Numerical *forecasts* with persistent boundary conditions and *forecast experiments* with boundary conditions linearly interpolated between surveys were performed. The real-time forecast successfully predicted the formation of the zonal jet prior to its observation. Dynamical interpolation shows unambiguously that the two anticyclonic eddies have merged and formed a single eddy. Even the forecast with incorrect boundary conditions demonstrates the internal dynamical processes involved in the merger event.

Two examples are given of four-dimensional data assimilation: direct insertion and a backward–forward combination technique. These results justify the use of the dynamical forecasts as synoptic time series. Parameter sensitivity experiments were performed to determine the sensitivity of the model to physical parameters such as stratification, to explore the dynamical balance, and to choose a reference level. The dynamics were found to be controlled by horizontal nonlinear interactions. A reference level of 1550 m was chosen. A set of energy and vorticity equations, consistent with quasi-geostrophic dynamics, were evaluated term by term for the forecast experiments. The evolutions of the streamfunction and vorticity fields are shown to be a three-phase (merging, expanding, and relaxation) process. Available gravitational energy increases due to buoyancy work; the merger event is interpreted as a finite amplitude barotropic instability process.

1. Introduction

We have been conducting a coordinated program of modeling and experimental research focused on the energetic and variable fields of jets and eddies associated with the California Current System in the deep northeast Pacific off the coast of northern California. The dynamics of this complex system are essentially not known and are of considerable interest, not only locally, but also because of the general mesoscale processes that occur. However, our greatest interest in the region is as a "test block" of ocean containing vigorous mesoscale eddies, which is relatively accessible logistically. Our research objectives relate to the methodology of obtaining optimal field estimates, i.e., carrying out accurate and efficient nowcasts and forecasts. These field estimates are useful for practical forecast purposes and for dynamical analysis in order to expose underlying physical processes.

Central to our research approach is the concept of the Oceanic Descriptive Predictive System (ODPS), constituted from a real-time observational network, a statistical model, and a dynamical model (Robinson and Leslie, 1985). By concentrating on a relatively small domain O(100–200 km) we were able to collect several independent synoptic realizations a year since 1982 (Mooers and Robinson, 1984; Reinecker et al., 1985), and the Harvard Open Ocean Dynamical model (Miller et al., 1983) has been set up in the region for forecasts, hindcasts, and simulations. Research issues include dynamical model initialization and verification with real data, data assimilation procedures, and the construction of mixed space–time statistical models for an anisotropic and nonstationary regime. The research program is called OPTOMA (Ocean Prediction Through Observation, Modeling and Analysis).

In the summer of 1983 we carried out three quasi-synoptic surveys (OPTOMA-V) in the region, each of about one week duration and two week separation, to provide two sets of model initialization and verification data. An important aim of the experiment was to carry out, for the first time, real-time forecasts. We did so

by radioing data from the ship to Monterey; the data was then relayed to computers at Harvard. The forecast results, which we reported previously (Robinson et al., 1984), were generally successful. Internal dynamical processes in the region rapidly altered the fields substantially; the model predicted the major features in the interior of the domain.

In this paper we present a detailed kinematical and dynamical study of the OPTOMA-V results. Section 2 presents the data, geostrophic analysis, objective mapping, and regular gridding procedures. Section 3 shows the objectively mapped fields. Dynamical forecasts obtained by initializing and running the dynamical model forward in time for a number of cases are presented in section 4. Section 5 summarizes the synoptic time series for the four-week period, which are constructed from the data via dynamical interpolation. Section 6 gives examples of data assimilation procedures, and section 7 studies the dependencies and sensitivities of results to variations in model parameters. Section 8 explores the dynamical processes governing the local evolution of the fields in terms of a quasi-geostrophically self-consistent energy and vorticity analysis scheme (EVA), and the conclusions are summarized in section 9.

2. Data acquisition and analysis

The high-resolution surveys for the forecast experiments were conducted by the R.V. *Acania.* The ship tracks were designed in the form of inner and outer star patterns to provide a fast initial view of the streamfunction and vorticity fields, followed by a larger scale realization (Fig. 1). The star-shaped pattern was chosen to allow the direct evaluation of the geostrophic velocity on a bounding strip, and thus a direct estimate of the vorticity. We were able to begin forecasting in a small domain when the inner star was completed. After completing the outer star pattern we could reinitialize in the larger region using the inner data for a most accurate initialization, or alternatively, we could reserve it for verification of an initialization with the outer data only.

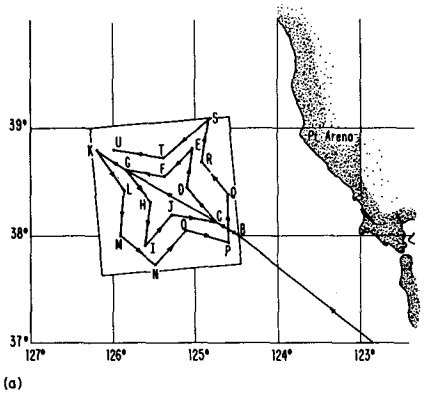

FIG. 1. The nominal cruise track for the Acania cruises. The forecast domain is a (150 km)^2 square centered at 38°20'N, 125°20'W, oriented 10 deg counterclockwise from true north.

The actual ship tracks are shown in Fig. 2 as modified by weather and feature exploration. Data samples were collected at 10 km spacing along the ship tracks; 450 m XBTs were interspersed with occasional 1000 m CTDs, which provided in situ temperature–salinity (T–S) information and deeper geostrophic shear. There was approximately 20 km spacing between ship tracks, somewhat smaller near the center of the domain and larger near the edges. This inhomogeneous sampling strategy allowed us to verify that the geostrophic motion was being adequately resolved. The two-week time interval between successive surveys was chosen to allow the flow to evolve somewhat between them (Mooers and Robinson, 1984). The length of the cruises were a compromise between the time available, the desire to cover a large domain, and the desire for a synoptic description. We obtained on legs 1, 2, 3: 89, 105, 96, XBTs and 5, 0, 14, CTDs.

a. Dynamic height and data extension

Here we describe how the data was handled after the cruises were finished; a detailed data report (Wittman et al., 1985) is also available. A T–S correlation was used to convert temperature profiles to more dynamically interesting density profiles. For this study the mean T–S correlation from CALCOFI (California Cooperative Oceanic Fisheries Investigation; Wyllie, 1966) was used. The mean T–S relationship computed from OPTOMA data gives quantitative but not qualitative differences. This is because the T–S relationship is stable except near the mixed layer, where heating is important, river-run off plumes often occur, and temperature inversions are common. Dynamic height was computed relative to 450 m and the mean dynamic height profile subtracted.

The dynamic height information, together with the assumption of geostrophy, gives us the velocity shear in the upper ocean. To obtain the deep ocean currents we make two assumptions. The first is that the density field throughout the water column is correlated so that variations in the deep density field are related to near-surface variations. Empirical Orthogonal Eigenfunction (EOF) analysis was used to describe the degree of vertical correlation of the density field. The first EOF contains most (>90%) of the variance in the vertical profiles of dynamic height computed from the deep CTDs (Smith *et al.*, 1985). By fitting the upper-ocean density field to the first vertical EOF mode, the density variations below 450 m (below the XBT data) were estimated and used to produce deep dynamic height fields.

The second assumption is about the amplitude of the barotropic component of the motion field, which is not directly measured by the density data. Deep current records from moorings somewhat to the north of our domain suggest that the deep ocean velocities are

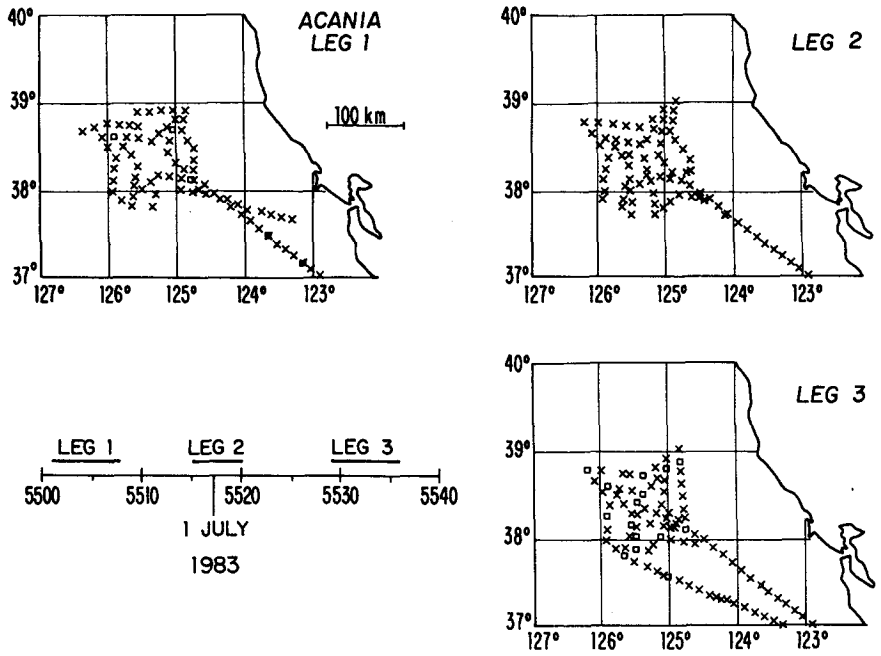

FIG. 2. Actual cruise tracks for the three *Acania* cruises. XBT stations are marked with an × and CTD stations with a box. The time line shows the span of each cruise in Julian days.

~5–10 cm s^{-1}, which are thus less than the surface velocities by almost an order of magnitude (Heath, 1983). This suggests that a deep-ocean zero-motion level would be appropriate. A 1550 m level of no motion was chosen for our central calculations; because of the shape of the EOF, this increases the surface motion by nearly 50% compared to the traditional choice of 450 m. One way of deciding which level to choose is to see which level leads to the most accurate forecast of the density field. We will adopt this approach later. A three-mooring array has recently been put in our domain to provide both upper-ocean and deep-ocean data to check our assumptions about the deep velocity field and its relationship to the thermocline flow.

b. *Objective analysis procedure*

Numerical forecasts require initial and boundary condition data on a uniform grid at all levels and each time step. For horizontal gridding we used a level-by-level objective analysis technique, which assumed the correlation to be homogeneous and isotropic, with correlation lags in both space and time (Robinson and Leslie, 1985; Carter and Robinson, 1986). We determined the spacial correlation scales from the dynamic height data by removing the data mean, then fitting the correlation with a functional form

$$C(\underline{x}_1, \underline{x}_2) = \left(1 - \frac{r^2}{az}\right) e^{-[r^2/(2b^2)]}, \quad r = |\underline{x}_1 - \underline{x}_2|, \quad (2.1)$$

adjusting a and b to best represent data pairs among data from the same cruise. The values chosen were $a = b = 75$ km. The functional form (2.1) was assumed because it represented the data well and excluded the possibility of developing negative definite correlation matrices, which may occur when the correlation form is determined simply from tabulating the data. The observed correlation from direct tabulation, surprisingly, did not appear to be significantly anisotropic. Attempts to remove bilinear trends from the individual cruise datasets led to unreasonably small correlation scales, probably because the individual cruises span an area not very much larger than the dominant scales of motion. Attempts to combine the three datasets in order to find a simple, useful dependence upon time lag, as we did in the POLYMODE region (Robinson and Leslie, 1985), were not successful. We therefore assumed the data to be perfectly correlated in time within each survey dataset and uncorrelated between datasets. The objective analysis procedure limited the number of observations used in the estimate of streamfunction to the five highest correlated. The instrument noise level was assumed to be 10% of the field variability. Typical estimated error after objective analysis is about 20% of the field variability.

The horizontal grid interval, 9.375 km, was chosen in order to resolve data variations at the smallest scale and to remain numerically efficient. Six levels were used in the vertical (50.0, 150.0, 400.0, 1066.6, 2150.0, 3390.0 m), which appear to be sufficient to resolve the motion of the shallow pycnocline and the vertical structure and dynamics of the dynamical modes. For

example, the first radius of deformation computed from high resolution density data is 25 km and from the numerical model is 26 km. The top three levels chosen are in the upper ocean where data is available.

3. Objective fields

The objectively analyzed fields for the three *Acania* cruises are shown in Fig. 3 using an assumption of zero motion at 1550 m to obtain the barotropic component as described in section 2a. The analysis domain is the $(150\ \text{km})^2$ domain of Fig. 1. All the data from each leg is lumped and plotted on the central day. The geostrophic pressure is related to the quasi-geostrophic streamfunction by proportionality factor $\rho_0 f_0$; the nondimensionalization of the streamfunction shown is given in section 6. Even in the upper layers where data is available, the streamfunction patterns are quite similar in the vertical, although the flow is surface intensified.

On Julian day 5506 the thermocline flow in the center of the region was very weak. A strong current, probably a segment of an anticyclonic eddy, flowed in the northeast corner; a 0.5 m s^{-1} southwestward current, probably part of a strong anticyclonic eddy, flowed in the northwest, and a segment of westward (cyclonic) flow existed along the southern boundary. Two weeks later the flow had changed dramatically; the center was dominated by a 60 cm s^{-1} zonal jet, the anticyclone in the northeast had disappeared and been replaced by a cyclonic segment, and the northwest anticyclonic segment had expanded. By day 5534 the northwest anticyclonic eddy was further enlarged and together with the current, now entering from the eastern region and oriented towards the southwest, filled the entire central and southern region with typical speeds $\sim$0.2 m s^{-1}. In a month the average speeds were reduced by more than a factor of two.

4. Dynamical forecasting and experiments

The numerical model is a baroclinic quasi-geostrophic model derived and tested in Miller et al. (1983) and described in Robinson and Leslie (1985). Besides initial and boundary conditions the model requires mean stratification averaged between streamfunction levels, bottom topography, a coefficient of linear bottom drag, and the order and frequency of application of the horizontal vorticity filter. The average stratification is obtained from the CALCOFI data. The coefficient of bottom drag is set to zero since the duration of the forecasts is too short for it to be important. A fourth-order Shapiro vorticity filter applied every time step is used to remove small-scale vorticity, which results from the enstrophy cascade and would eventually cause numerical instability. Bottom topography is used in the forecasts and forecast experiments; the particular region chosen avoided seamounts and steep slopes.

Real-time forecasts and simulations of real-time forecasts were performed by initializing the dynamical model with the analyzed data and simply persisting the boundary conditions. In the POLYMODE region of the western North Atlantic the time dependent correlation has been used to forecast boundary conditions statistically, which is much better than persistent boundary conditions. Here, because of the strong events and rapid changes observed during these cruises, a useful time-dependent correlation was not available, as mentioned above.

Additionally, we performed a posteriori forecast experiments in which the boundary conditions were linearly interpolated between successive cruises. The numerical model in this case is used as a dynamical interpolator to fill in the motion interior to the domain in a way that is consistent with the equations of motion.

a. Day 5506–5520

The forecast using the first survey as initial conditions and persistent boundary conditions is shown in Fig. 4a. The anticyclones in the northwest and northeast both move into the region and merge to form a strong zonal jet. The anticyclone in the northeast has entirely disappeared by 5514, but a manifestation of the northwest eddy remains. Because of the incorrect (persistent) boundary conditions, the flow near the boundary does not agree well with observations (Fig. 3) by day 5520. However, we can see that intense internal dynamical processes have caused a radical change in the internal flow pattern between 5506 and 5520, which is in general agreement with observations.

The forecast experiment (Fig. 4b) shows that the anticyclone originally in the northeast weakened to half its original strength by 5516, with the northwestern eddy weakening as well. By 5514 the zonal jet had developed and a small cyclone formed in the northeast. The eddies expand and the jet persists. On day 5520 the general flow pattern is in very good agreement with the observations (Fig. 3).

These results show the power of the numerical model as an interpretive tool. Without the dynamical model it is difficult to unambiguously interpret the transition of the motion field from 5506 to 5520. Using the model as a dynamical interpolation device, the eddy merger event is clearly indicated.

b. Day 5520–5534

The persistent boundary-condition forecast beginning at leg 2 (Fig. 5a) shows the anticyclonic feature to develop with the passage of time. The east–west high pressure feature evident at Julian day 5520 separates by 5534, again leaving the strong anticyclonic feature in the northwest and strengthening the cyclone in the northeast, which is constrained to remain in the do-

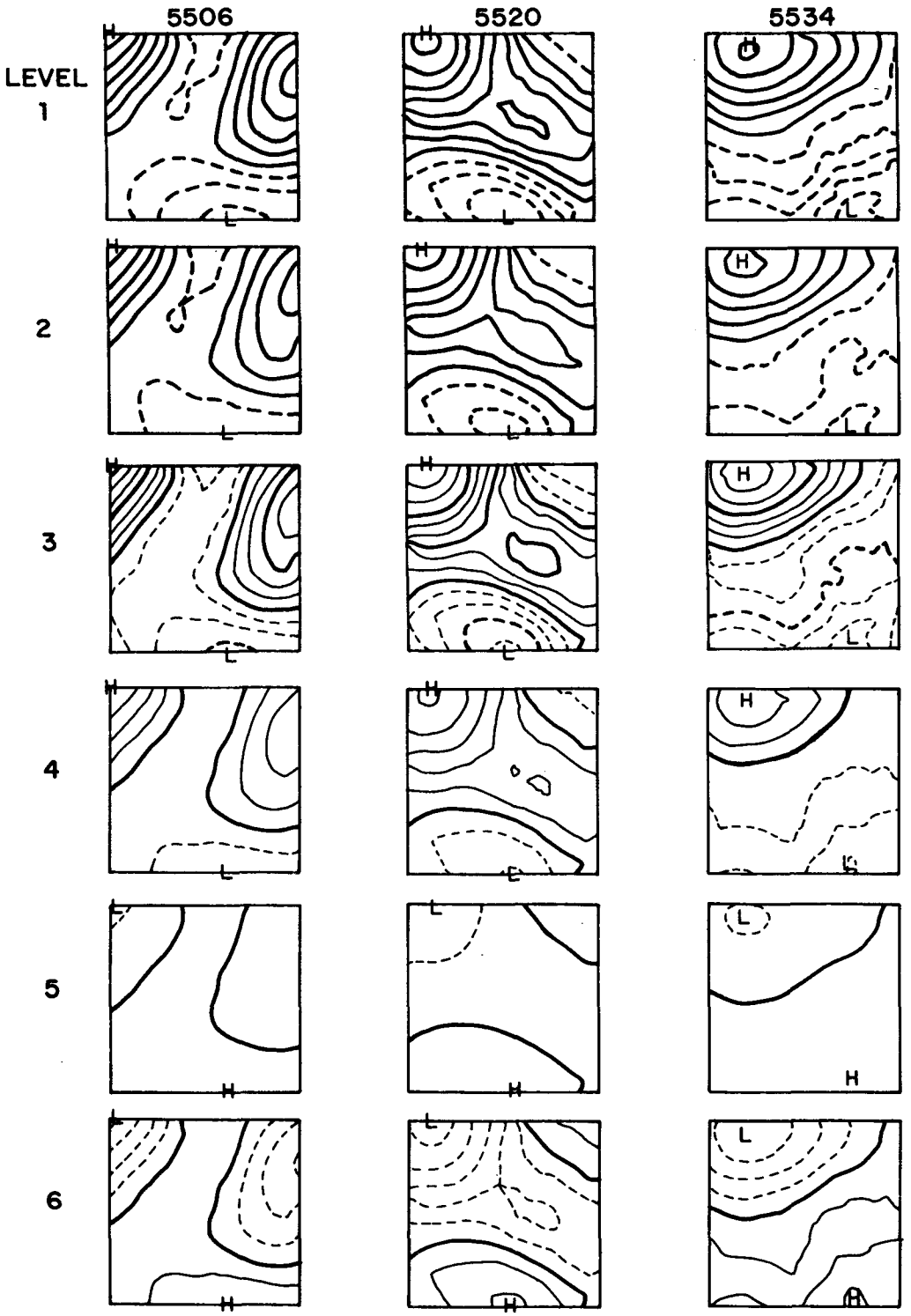

FIG. 3. Streamfunction computed at the central date of each cruise (5506, 5520, 5534) at each model level. The level depths are 50, 150, 400, 1066.6, 2150 and 3390 m. The procedure described in the text has been used to extend the streamfunction into the deep ocean. The contour intervals are 0.75, 0.75, 0.25, 0.125 and 0.125.

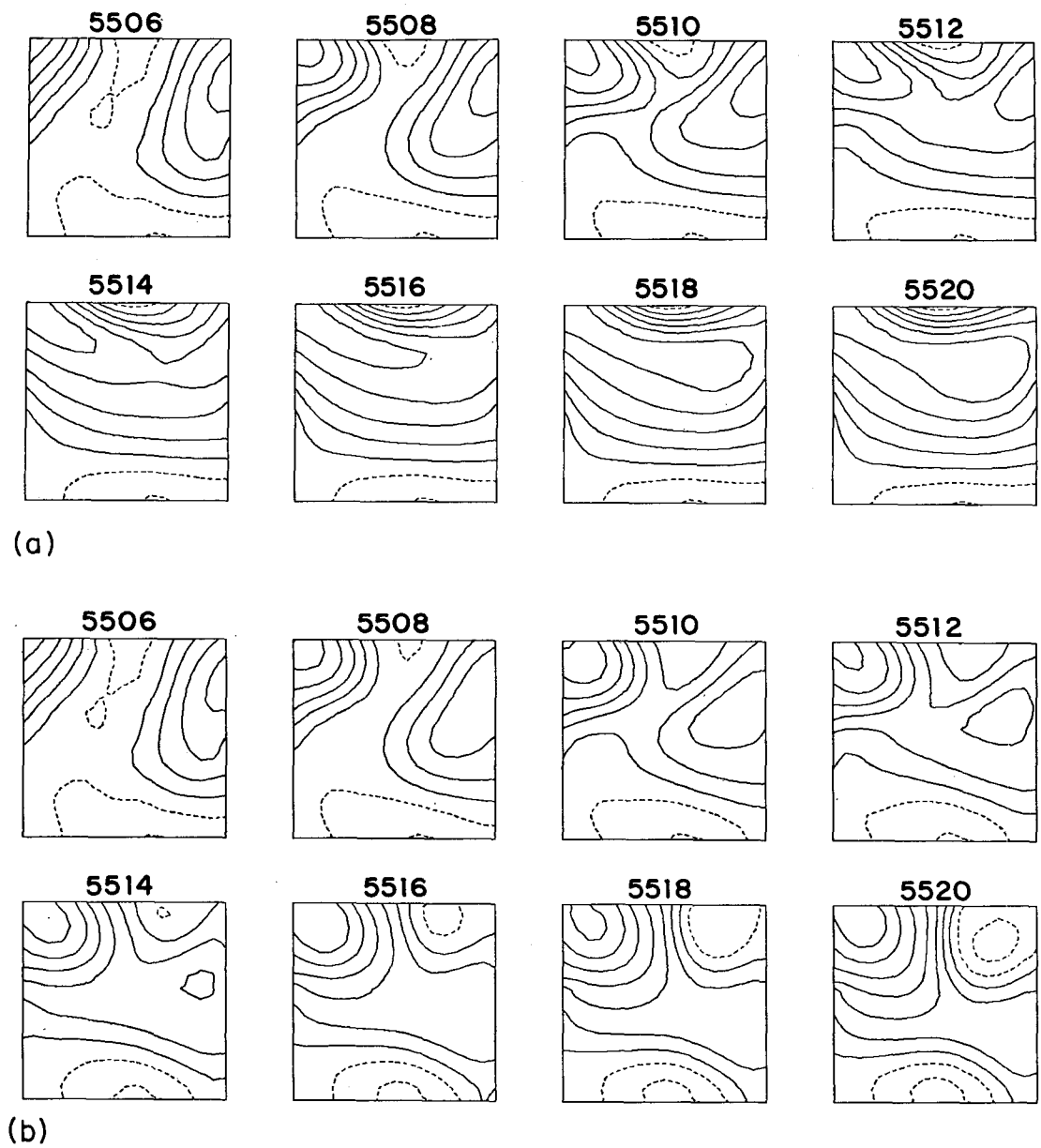

FIG. 4. Streamfunction at 150 m beginning on 5506 for two weeks. (a) *Forecast* with persistent boundary conditions and (b) *forecast experiment* with linearly interpolated boundary conditions. The contour interval is 0.75.

main by the persistent boundary conditions. The strong anticyclonic feature in the northwest expands toward the south and is more elongated than in the objectively analyzed field at 5534.

The linearly interpolated boundary-condition forecast experiment shows (Fig. 5b) the northwest anticyclone absorbing all of the region's negative vorticity into one spatially large, but finally not more intense, feature with an enclosed high. The segment of the low in the persistent boundary forecast is weaker and almost disappears. Comparison with the observed fields again is very good.

In both the forecast and forecast experiment, the major event during this two-week period is the development of the dominant anticyclone and its expansion toward the southeast to occupy most of the domain. Even with the incorrect boundary conditions, the merger of the two eddies is reproduced by the model. Thus the internal dynamical processes work successfully to provide the general character of the event. In the forecast experiment, the expansion ceases at about day 5528, after which the anticyclone recedes and becomes somewhat rounder. During this latter shaping process of the eddy, the zonal jet disappears.

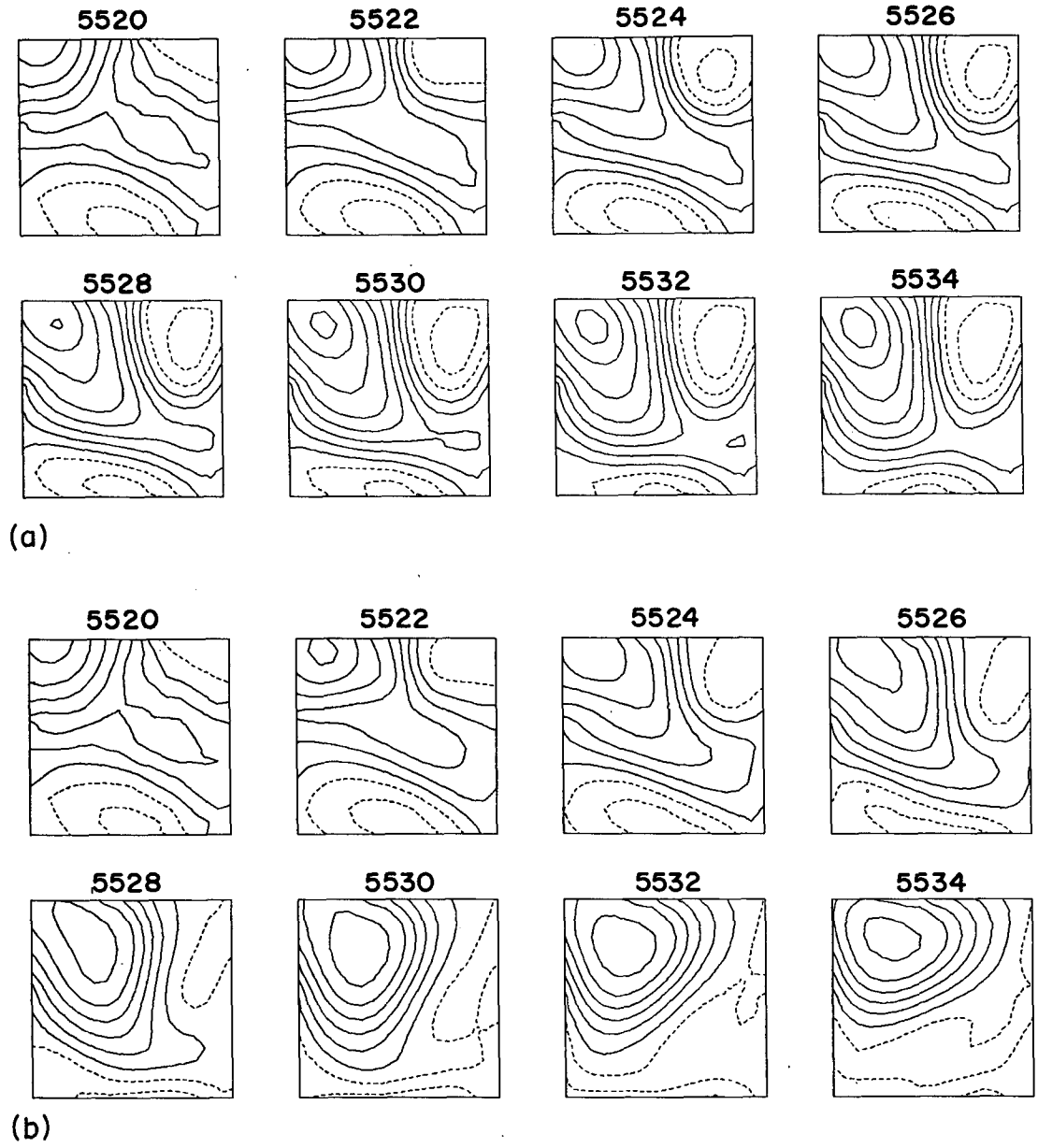

FIG. 5. As in Fig. 4 except for the two-week period beginning 5520.

c. Analysis of difference fields

The difference fields in Fig. 6 are the differences between the forecasted streamfunctions (Figs. 4a, b; 5a, b) and observed fields of Fig. 3 for the four cases. We use the term "difference field" here rather than "error field" to stress the fact that sources of both errors and accuracies exist in both field estimates. For example, an accurate dynamical interpolation could give an improved field estimate over lumped asynoptic data. The difference field for the forecast experiment beginning on 5506 shows the forecast cyclonic feature in the northeast to be somewhat more intense, and the anticyclonic feature in the northwest to be broader, than the objectively analyzed features. The difference field for the forecast experiment beginning on 5520 shows the anticyclonic eddy to be stronger and broader than the analyzed observations. Figures 6b, d are ringed by boundary-error induced features that invade our relatively small domain. The large-scale features of Figs. 6b and 6d we call the "dynamical adjustment" fields and their highs appear still identifiable in 6a and 6c, respectively.

In order to quantify the difference between the predicted and observed fields we introduce two scores to estimate the accuracy of a forecast by comparing the

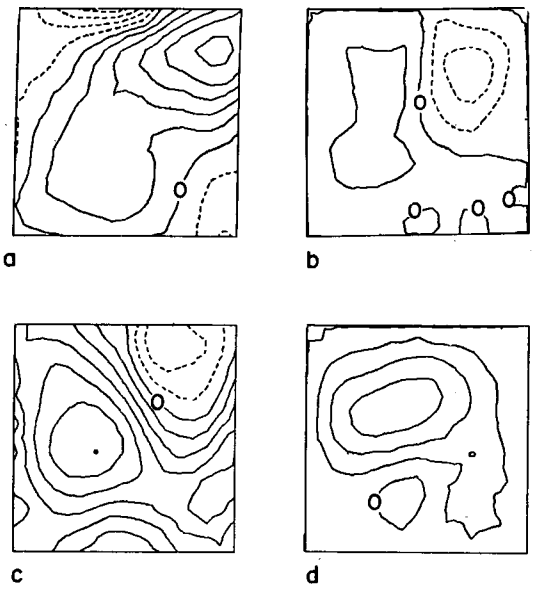

FIG. 6. Difference fields for the four forecasts. (a) and (b) show the difference between the forecast streamfunction in Figs. 4a, b at 5520 and measurements. (c) and (d) show the difference between the forecast streamfunction at 5534 in Figs. 5a, b at 5534 and measurements. The contour interval is 0.75.

predicted density in the thermocline, $\hat{d}_{ij}$, with the observed density d_{ij}, where the subscripts refer to the spatial location of the measurement. Density fields are compared since they are more directly measured. They were calculated at the interfaces between 50, 150 and 400 m streamfunction levels. Both density fields have had their spatial means removed to prevent biasing. These scores are

$$\text{rms} = \frac{\langle(\hat{d} - d)^2\rangle^{1/2}}{\langle d^2\rangle^{1/2}}$$

$$\text{cor} = \frac{\langle \hat{d}d\rangle}{(\langle \hat{d}^2\rangle\langle d^2\rangle)^{1/2}}$$

where angle brackets represent spatial averaging.

If the analysis fields and the forecast were perfect, then the root mean square (rms) difference between the density fields would be 0.0 and the correlation (cor) would be 1.0. The forecast scores should be compared with the scores obtained by comparing objective maps from successive cruise legs. The values for rms and cor at 100 m between the leg 1 and leg 2 *observed fields* are (0.93, 0.44), and between leg 2 and leg 3 observed fields are (0.76, 0.73). These are the scores we obtain using a prediction scheme which assumes that the flow persists without changing between legs. The large values of rms and small values of cor quantify the degree of flow evolution between cruises. The scores of the forecasts will be discussed in section 7b.

5. The synoptic fields

It is apparent that during the four-week period the eddy fields in our experimental domain evolved rapidly and that the changes involved vigorous internal dynamical processes. The dynamical experiments shown in Figs. 4b and 5b present definitive synoptic time series, elucidating the behavior of the flow. The *dynamical interpolation* inherent in this representation is essential to the description of the fields; dynamical model initialization with real ocean data is a useful tool for modern synoptic oceanography. The robustness of the description given by Figs. 4b, 5b to alternative methods of melding data and forecasts will be demonstrated in section 6, and the internal dynamics will be elucidated in sections 7 and 8.

The general features of the evolution of the flow as revealed by the pressure (streamfunction) fields are usefully summarized in three phases.

PHASE 1: *Merger* (5506–5515)

The two original eddy segments merge, strengthening the northwest anticyclone and eliminating the northeast cyclone. The zonal jet is formed, and a northeast cyclone appears.

PHASE 2: *Expansion* (5516–5526)

The northwest anticyclone expands into the domain; the westward-flowing zonal jet is fed by a southward-flowing jet emanating from the center of the northern boundary. (The model may be somewhat "faster" than nature since comparison of days 5520 of Figs. 4b and 5b show the northwest anticyclone expanded further into the domain and the northeast cyclone stronger in the first picture. Keep in mind that the data of 5520 is lumped.)

PHASE 3: *Relaxation* (5527–5534)

The swirl of the large anticyclone retreats to the northwest (although the pressure center advances); the intense and looping jet flow relaxes to a broad flow associated with the eddy swirl, giving a rounded shape to the remaining eddy.

6. Data assimilation

In the preceding calculations the observations entered the forecasts only through the initial conditions and boundary conditions. To make the fullest use of asynoptic observations they should be directly introduced into the forecast model at their time and place of measurement. Procedures for four-dimensional data assimilation suitable for special oceanic nowcasting and forecasting require careful research and development. In this section we give two simple examples of field estimates utilizing this principle.

We explored the effect of asynoptic data acquisition on the forecast in our first example. The model was first integrated backward in time from 5506 to 5501, the first day of sampling in the star pattern. We then integrated forward, introducing data into the model by

a direct insertion method; new density data replaced the model estimate at the nearest grid point. A persistent boundary condition forecast was made up to day 5520, the central point in leg 2. The resulting forecast is quite similar to the forecast of Fig. 4a, providing evidence that the measurements within each cruise may be assumed to have been taken simultaneously for this purpose. Also, data point insertion may not influence the model forecast strongly.

Measurements have information not only about how the flow will evolve after the measurements were made but also about how the flow evolved before the measurements were made. A most important use of four-dimensional (4-D) assimilation is to improve the field estimate during the period of data acquisition. In an attempt to improve our field estimates, two forecasts were combined. The first is the *forward* forecast experiment with linearly interpolated boundary conditions Fig. 4b. The second is a forecast experiment which begins with the observed field at the beginning of the second forecast $T_1 = 5520$ and runs *backward* in time, again using linearly interpolated boundary conditions to $T_0 = 5506$. Filtering in both cases acts to remove small-scale vorticity. The two forecasts beginning at T_0 and T_1 are linearly combined

$$\psi(t) = \frac{(t - T_1)}{(T_1 - T_0)} \psi_{\text{forward}} + \frac{(T_0 - t)}{(T_0 - T_1)} \psi_{\text{backward}}$$

so that a uniform space–time series (Fig. 7) is produced which is both consistent with the cruise data objective analysis, Fig. 3, and strongly constrained by the forecast model (compare Figs. 4b, 5b, and 7). A similar set of experiments have been performed between 5520 and 5534. This space–time series represents our best estimate of how the field evolves from leg 1 to leg 3. The close match of the series to the forecast experiments means that energy and vorticity analyses may be performed on the quasi-geostrophically consistent forecast fields with confidence.

7. Parameter and sensitivity studies

The numerical model integrates the potential vorticity equation, which in nondimensional form is

$$\frac{\partial}{\partial t}[\nabla^2\psi] + \frac{\partial}{\partial t}[\Gamma^2(\sigma\psi_z)_z]$$
$$= -\alpha \mathbf{V}\cdot\nabla\nabla^2\psi - \alpha\Gamma^2\mathbf{V}\cdot\nabla(\sigma\psi_z)_z - \beta\psi_x + \mathbf{F} \quad (7.1a)$$

and symbolically

$$\dot{Q} = \dot{R} + \dot{T} = \Delta F_R + \Delta F_T + \Delta F_p + \mathbf{F} \quad (7.1b)$$

here $\mathbf{V} = -\mathbf{k} \times \nabla\psi$, $\alpha = t_0 V_0/d$, $\beta = t_0\beta_0 d$, $\Gamma^2 = (f_0 d/N_0 H)^2$, and $\sigma = N_0^2/N^2(z)$. Equation (7.1b) gives the notation we will use to refer to the corresponding terms in (7.1a). Here, R indicates relative vorticity, T thermal vorticity (the stretching term), Q the total vorticity, ΔF an advective flux divergence (relative, thermal and planetary) and $\mathbf{F}$ is the filter. Also, Γ^2 measures the relative importance of T and R processes, and α measures the strength of nonlinear advections relative to local time changes. The dimensional scaling values chosen are $t_0 = 1.0 \times 10^6$ s, $d = 50$ km, $\beta_0 = 2.0 \times 10^{-11}$ m^{-1} s^{-1}, $V_0 = 0.1$ m s^{-1}, $f_0 = 0.89 \times 10^{-4}$ s^{-1},

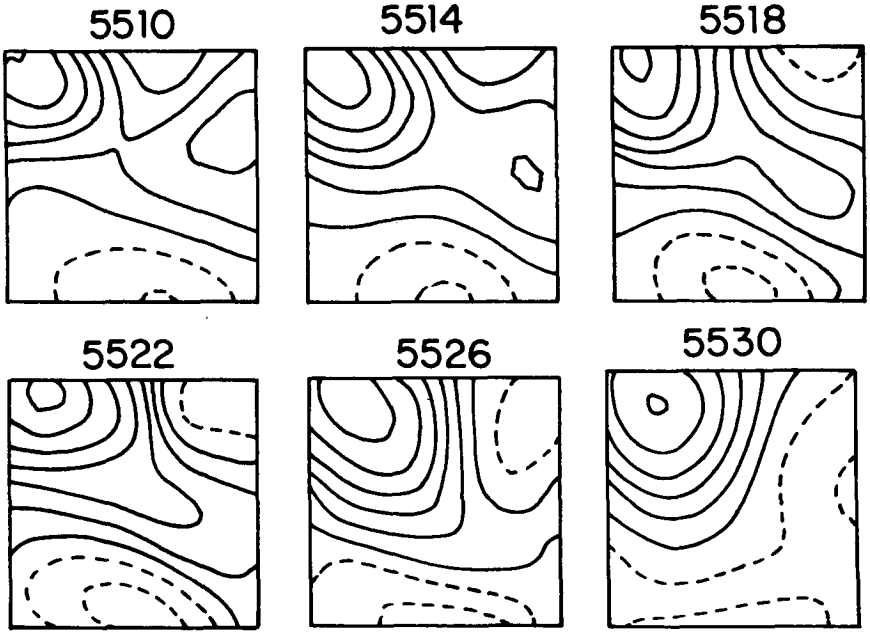

FIG. 7. Time series of the streamfunction at 150 m created by integrating the model both forward and backward in time and combining the forecasts as discussed in the text.

$H = 150$ m, $N_0 = 0.011$ s^{-1}, so $\alpha = 1.998$, $\Gamma^2 = 7.27$, $\beta = 1.10$; $\psi_0 = V_0 d$. Topographic shapes consistent with quasi-geostrophy are allowed in the bottom boundary condition. In the experiments of this and the next section, however, a flat bottom was used, since the absence of topographic slopes caused no significant changes in the forecasts.

In this section we examine the dependence upon, and sensitivity of the model dynamic forecasts to, changes in the parameters. The purpose of the parameter study is that the basic physical processes governing the central case of interest are clarified by such a study. The experimental values are of course well determined. Additionally, it is important to establish the robustness (or nonrobustness) of forecasting results to quantitative choices of parameters. This is essentially equivalent to a study of bias in the initial and boundary condition data.

a. Nondimensional parameters

A list of the experiments is given in Table 1 and illustrated in Fig. 8. Recall that in the central case of dynamical interpolation (Figs. 4b, 5b and 8a) the original northwest and northeast eddies merge and expand, after which the northwest anticyclone survives and the zonal jet is formed. By day 5512 the merger as indicated by the streamfunction field is well under way; it has been completed by day 5516, and on 5520 the expansion of the anticyclone is occurring.

In the first experiment we set the nonlinear terms to zero ($\alpha = 0$). Comparing Figs. 8a, b the anticyclonic eddies are seen to remain separated throughout the forecast, with only slow changes in intensity and position. The nonlinear terms dominate the dynamical evolution and merger. This interpretation is strengthened by experiment 2, Fig. 8c. Increasing α causes the merging to occur early in the forecast, before 5512, and by 5520 the anticyclonic feature has unrealistically intensified and expanded, filling the entire domain. Decreasing Γ^2 by a factor of five (e.g., increasing the stratification) reduces the importance of vortex stretching terms (thermal compared to relative vorticity effects). The result is also a faster merging at all levels (experiment 3, Fig. 8d). Results are similar to experiment 2 but somewhat slower. Increasing Γ^2 by a factor of five (experiment 4, Fig. 8e) causes the merger and jet formation to occur more slowly but gives a forecast closer to the central case than the previous experiments. In experiment 5 (not shown) the relative vorticity term ΔF_R is reduced compared to the stretching term ΔF_T, while $\dot{T}$ is increased compared with $\dot{R}$. The result is that merging is delayed at least beyond 5520.

Together these experiments clearly indicate that the merging process is nonlinear and controlled by the relative vorticity terms, although baroclinic effects are not negligible to give realistic shaping of the eddy during the expansion phase. However, during the merger phase the enhancement of Γ^2 baroclinic effects slows down the horizontal nonlinear vorticity and energy cascade. The dependence upon α is stronger than upon Γ^2, and β effects are not important in the cases studied. The detailed vorticity and energy balances for the central case are presented in the next section. Experiments changing the order of the filter only change the smaller scale related to the enstrophy cascade; some filtering is needed for numerical stability.

TABLE 1. Parameters chosen for the sensitivity experiments.

Experiment	Γ^2	α	β
0. Central	7.27	2.0	1
1. Linear	7.27	0.0	1
2. Advective	7.27	4.0	1
3. Relative	1.4	2.0	1
4. Thermal	36.3	2.0	1
5. Linear Relative–Nonlinear Thermal	145.0	0.1	1

b. Zero motion level

The zero motion level for the forecast initial and boundary conditions cannot be determined directly from the data. In order to determine the dependence upon the assumed level of no motion, we performed forecast experiments, from legs 1 to 2 and also 2 to 3, for five levels of no motion located throughout the water column and also for a case in which the flow was unidirectional throughout the water column. Table 2 shows the scores for the forecast of the upper and midthermocline density field for these experiments. The level which leads to the most accurate forecast based on our measures of error at 100 and 275 m is a 1550 level of no motion. Considerably poorer forecasts occur with either very shallow, very deep or virtual (the bottom currents positively correlated with the surface currents) zero-motion levels. This was the basis of our selection of 1550 m for our central case. Of course, the model is not very sensitive to the exact value chosen.

8. Dynamics

In this section we describe the combined use of model forecasts and local analyses of energy and vorticity budgets to interpret the nonlinear processes which control the dynamics of the merger event and subsequent development. The forecast experiments create a complete data set of quasi-geostrophically adjusted fields, which can be used to evaluate energy and vorticity balances as a function of space and time. The model dynamically interpolates between data and produces streamfunction fields that contain the essential features of the data fields of Fig. 3 and are also consistent with conservation of potential vorticity Eq. (7.1). We can then consistently evaluate the vorticity and energy fluxes and their divergences on this model dataset.

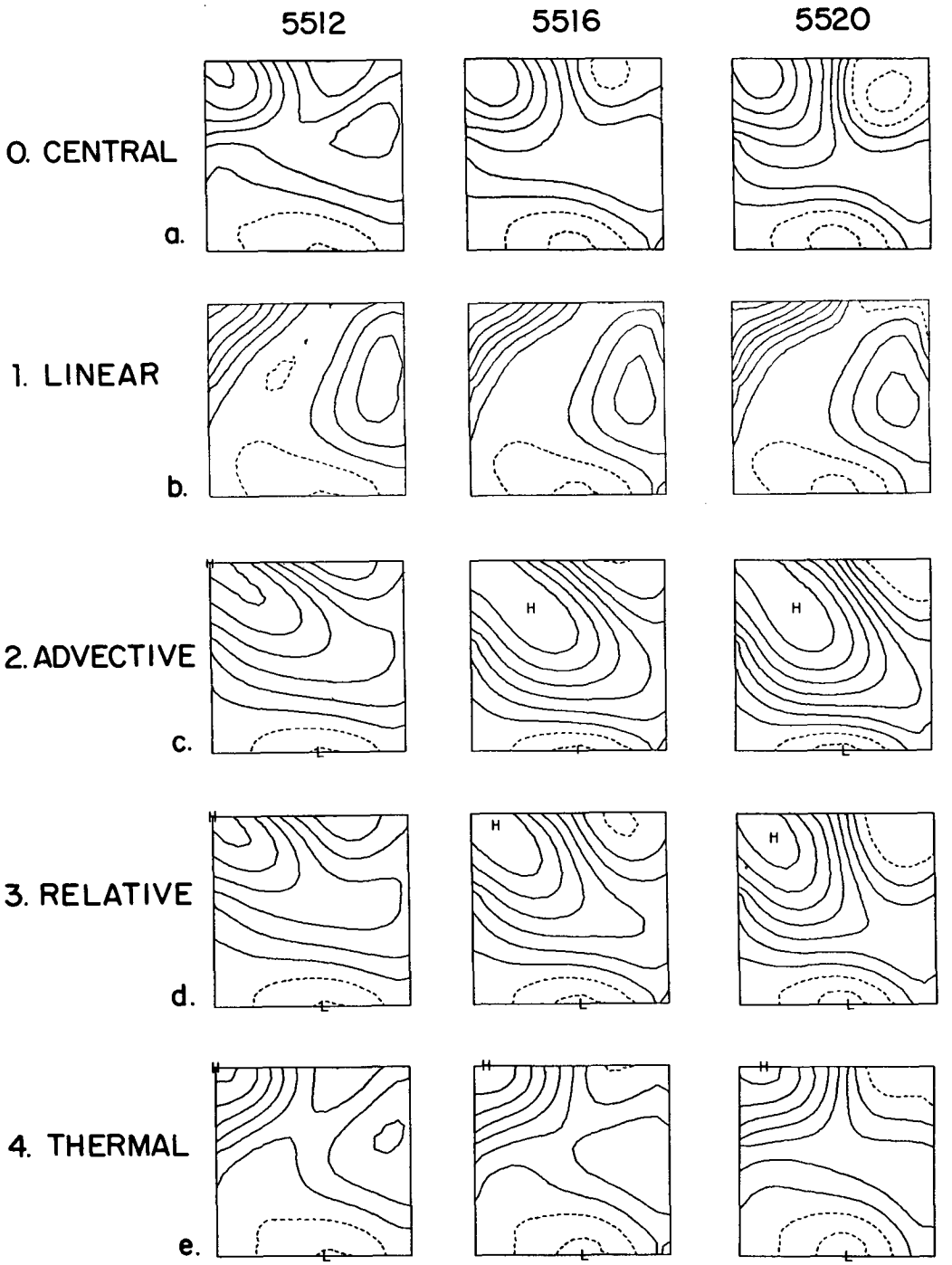

FIG. 8. Parametric dependence and sensitivity of the forecast experiment streamfunction beginning 5506. The parameter values are given in Table 2. Contour interval is 0.75.

Our approach to the energy dynamics of the quasigeostrophic system parallels the traditional development of the vorticity dynamics. The energy equations are formed from the full momentum and buoyancy conservation equations, and the basic Rossby number expansion is inserted. The zero-order energetics simply state that the geostrophic pressure work flux does not diverge. The first-order equations contain terms in the first-order pressure, but by evoking zero-order geostrophy, these can be relegated to a divergence-free flux only. The details are given by Pinardi and Robinson (1986).

TABLE 2. Forecast errors for different choices of zero motion level. Two measurements are given a correlation and a root-mean-square deviation of the forecast from the observed density field for two depths.

Forecast dates	Correlation 100 m	Correlation 275 m	rms 100 m	rms 275 m	Zero motion level	Integrated energy for level 6
5506–5520	0.595	0.624	0.821	0.826	200	2.3
	0.843	0.958	0.554	0.286	500	2.9
	0.969	0.941	0.246	0.365	1550	0.9
	0.979	0.918	0.207	0.440	4000	0.8
	0.967	0.886	0.254	0.531	*	4.1
5520–5534	0.711	0.668	0.706	0.748	200	2.3
	0.921	0.759	0.399	0.704	500	3.0
	0.960	0.905	0.282	0.507	1550	1.0
	0.962	0.923	0.272	0.452	4000	0.05
	0.953	0.948	0.302	0.328	*	2.3

* These runs initially have the same strength currents as in the 500 m case except that they are positively correlated with the surface currents.

The prognostic kinetic and available gravitational equations for the zero-order flow are written in the following equivalent forms:

$$\frac{\partial}{\partial t} K_0 = -\alpha\nabla\cdot(\mathbf{u}_0 K_0) - \nabla\cdot(p_1\mathbf{u}_0 + p_0\mathbf{u}_1) - (p_0 w_1)_z + \delta_0 w_1 + \mathbf{D} \quad (8.1a)$$

$$\frac{\partial}{\partial t} K = -\alpha\nabla\cdot(\mathbf{u}K) - \nabla\cdot(p\mathbf{k}\times\mathbf{u}_t + \alpha p\mathbf{u}\cdot\nabla(\mathbf{k}\times\mathbf{u}) - \beta y p\mathbf{u}) + (p\sigma p_{zt} + p\alpha\sigma\mathbf{u}\cdot\nabla p_z)_z + p_z w + \mathbf{D} \quad (8.1b)$$

$$\dot{K} = \Delta F_k + \Delta F_\pi{}^t + \Delta F_\pi{}^a + \Delta F_\pi{}^\beta + \delta f_\pi{}^t + \delta f_\pi{}^a - b \quad (8.1c)$$

$$\frac{\partial}{\partial t} A_0 = -\alpha\nabla\cdot(\mathbf{u}_0 A_0) - \delta_0 w_1 \quad (8.2a)$$

$$\frac{\partial}{\partial t} A = -\alpha\nabla\cdot(\mathbf{u}A) - p_z w \quad (8.2b)$$

$$\dot{A} = \Delta F_A + b \quad (8.2c)$$

where the subscripts in (8.1a) and (8.2a) indicate the order in the quasi-geostrophic expansion of the kinetic and available gravitational energy equation. The notation is the following: $K_0 = (u_0{}^2 + v_0{}^2)/2$, $A_0 = \sigma(\delta_0/2)^2$, $\mathbf{u}_0 = -\mathbf{k}\times\nabla p_0 = -\mathbf{k}\times\nabla\psi$, $\delta_0 = p_{0z}$. Here, **D** is a dissipative term related to the small but sometimes locally nonnegligible effects of vorticity filtering, **F**. In Eqs. (8.1b) and (8.2b) the subscripts have been dropped and the terms are all expressed in terms of the geostrophic pressure and velocity fields. Comparison of the terms in Eqs. (8.1a) and (8.1b) allow a direct interpretation of the terms in Eq. (8.1b). Equations (8.1c) and (8.2c) show the symbols used in the figures to represent each contribution in the two equations. The superscript notations (t, a) refer, respectively, to local time rate of change and advective contributions to first-order ageostrophic effects. The relationship of this approach to the energetics of the quadratic invariant obtained directly from (7.1) is given in Pinardi and Robinson (1986).

The vorticity equation terms (7.1) are evaluated with finite elements in the horizontal and finite difference in the vertical as in the model runs of Miller et al. (1983). A finite difference fourth-order scheme is used in the horizontal to evaluate the derivatives in (8.1a) and (8.2a) and centered time differencing is used for the time rate of change. Finite differencing in the vertical is used consistent with the model numerics.

We will first present and interpret instantaneous maps of the terms in the Eqs. (8.1b), (8.2c) and (7.1) for the forecast experiments described previously. We then will compute time series of horizontally averaged terms in the same equations for a chosen domain of integration. Finally, vorticity and energy diagrams will be introduced for the time- and space-averaged terms of the vorticity and energy equations to describe the net gains, losses, interactions, and internal conversions in the system during the evolution of the flow from Julian day 5506 to 5534. We call our energy and vorticity analysis method EVA.

a. Local vorticity analysis

The total dynamical vorticity Q, relative vorticity R and thermal vorticity T maps are shown in Fig. 9 at different times for the two forecast experiments, Figs. 4b and 5b. At level 2 thermal and relative vorticity are of approximately equal magnitude, while at level 3 Q is approximately R. From the vorticity maps it is evident that the streamfunction (pressure) merger event of Julian day 5510 precedes the total vorticity Q merger event. The thermal vorticity merges at the same time as the streamfunction, but R merges later (~5520). These vorticity maps show the three phase processes of section 5 and provide additional dynamical insight.

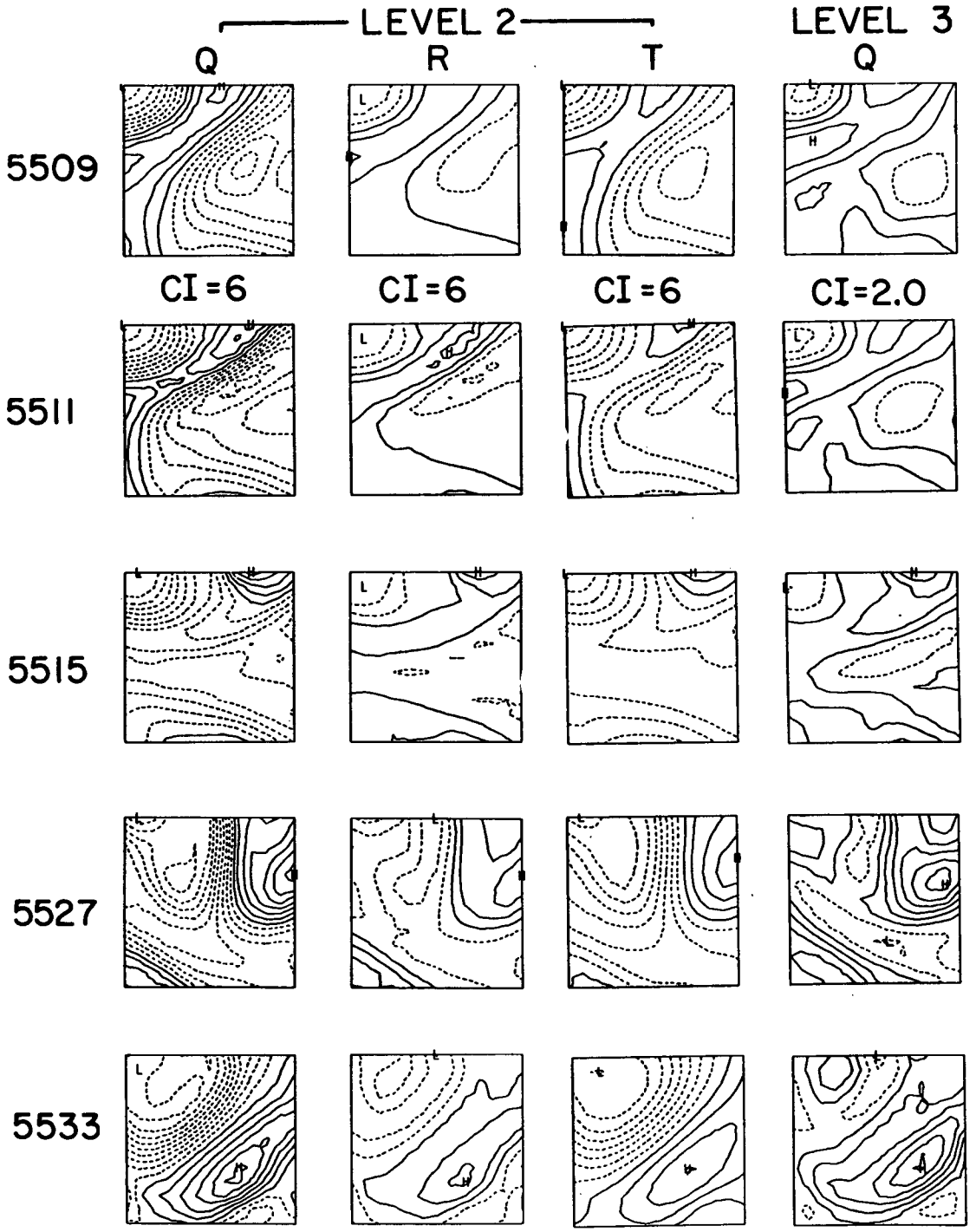

FIG. 9. Maps of the total (Q), relative (R) and thermal (T) vorticity at selected days during the forecast experiments. At level 3 the thermal vorticity is small so that the total and relative vorticities approximately balance. This figure and the following figures use a 112.5 km inner domain.

Figure 10 maps the terms of Eq. (7.1), which contribute significantly to the eddy scale vorticity balance. The effect of the filter is discussed below. The overall balance is between $\dot{R}$, ΔF_R, and separately between $\dot{T}$ and ΔF_T during the first two phases. The last phase of the process is a balance between ΔF_T and $\dot{T}$ with ΔF_R and $\dot{R}$ contributing only at smaller scales.

During the first phase, in the neck between the two

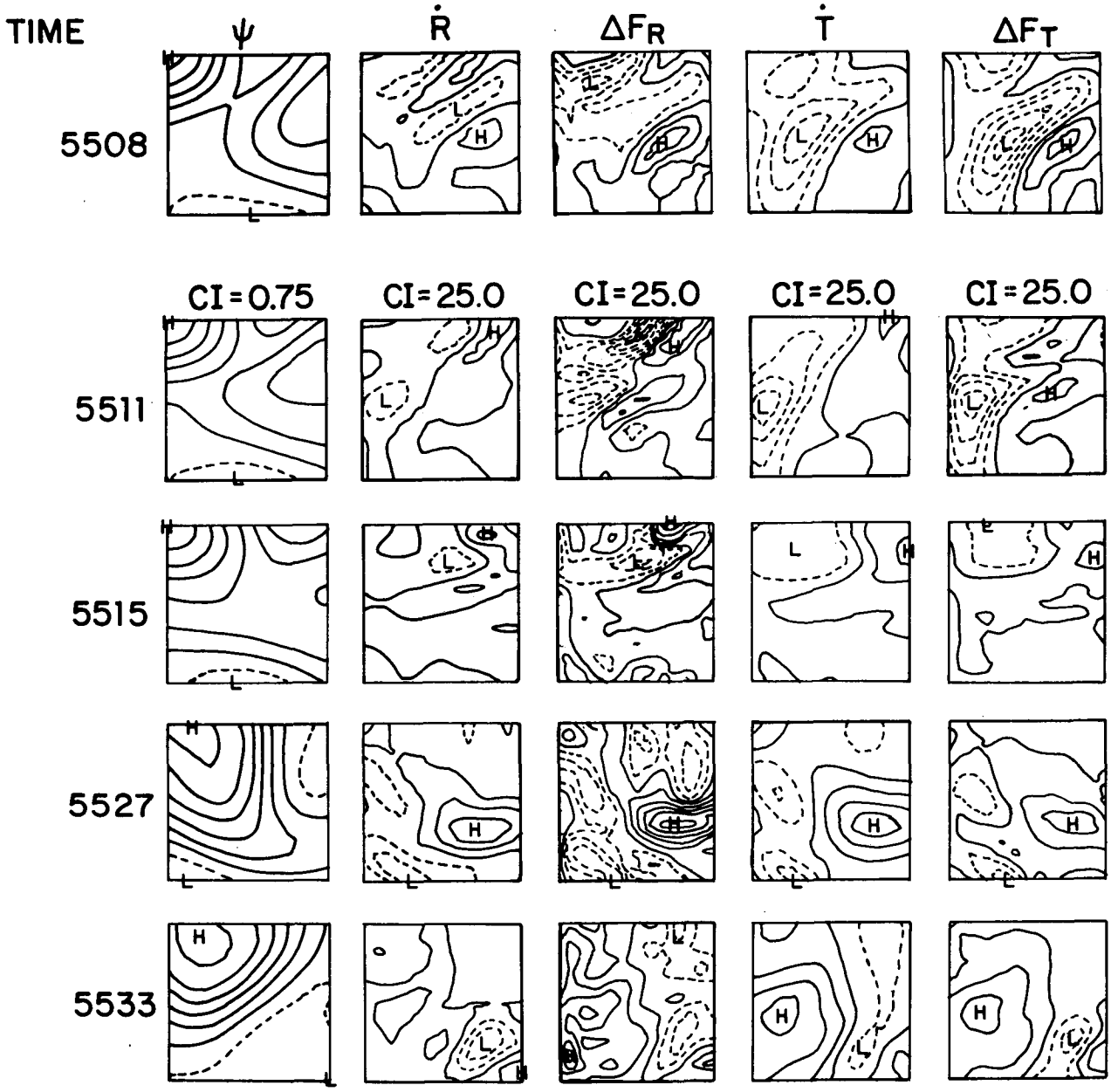

FIG. 10. Terms from the prognostic vorticity equation (7.1) computed from the forecast experiment at level 2.

merging eddies, ΔF_R is largest and is balanced by $\dot{T}$, ΔF_T and filter, F. During the development phase ΔF_R in the region of merging is always strong. At level 3, not shown here, the merging process is 2–3 days faster than at level 2 and the only important terms are ΔF_R and $\dot{R}$, which are almost in perfect balance all the time; $\dot{T}$ is smaller and the filter contributes as at level 2.

The interpretation of the vorticity dynamics is then straightforward: the merging and development phase is indicated by a major contribution from ΔF_R, which is mainly balanced by $\dot{T}$, ΔF_T and filter. There is an enstrophy cascade to small scales since the filter is very active, especially during merging and development. At level 3, where the balance is only between $\dot{R}$, ΔF_R and filter, the merging occurs more rapidly and involves more streamlines than at the upper level. This shows that the merging is primarily due to horizontal nonlinear vorticity dynamics, which subsequently induces a change in the thermal vorticity by deepening the isotherms in the region of merging. This interpretation is supported by the parameter variation experiments of Table 1, where we have shown that the enhancement of the merging process occurs with a stronger ΔF_R term with respect to ΔF_T (Experiment 3). It is also evident

from experiment 4 that strong $N^2(z)$ inhibits the merging process during the first phase and the beginning of the second.

b. Local energy analysis

Here we analyze the kinetic and available gravitational energy balances. Figures 12 and 13 show the important terms in the balances on three days chosen to illustrate the different behaviors energetically that occur during the three "vorticity phases" discussed in the last section.

The pressure work flux, $\Delta F_\pi = \Delta F_\pi^t + \Delta F_\pi^a + \Delta F_\pi^\beta$, is always important to the K balance, but of these terms only ΔF_π^a is significant. In Fig. 11 the zonal and meridional contributions to ΔF_π^a are shown. During the initial merger phase energy converges in the domain mainly by $\Delta_y F_\pi^a$ in the northwest corner. This behavior is dominant at all levels. During the expansion phase $\Delta_y F_\pi^a$ and $\Delta_x F_\pi^a$ increase, generally opposite in sign, and individually are larger in magnitude than other terms in (8.1). The residual total ΔF_π^a can be seen from Fig. 13 to be converting to A via buoyancy work. Finally in the relaxation phase the ΔF_π^a components weaken and become wavelike at somewhat smaller scales.

The spatial distribution of kinetic energy, K (Fig. 12) differs markedly during the three phases; K is never numerically significant to the balance of (8.1). During the first phase the balance is characterized by relatively small contributions from ΔF_k, ΔF_π and δf_π. During the expanding phase all four terms shown in Fig. 12 grow; ΔF_k converges energy in the region; ΔF_π partly balances this but also exhibits smaller scales, which are "dissipated." Note that our vorticity filter related dissipation is locally either a source or sink. By the start of the relaxation phase, the balance starts to be between ΔF_π and ΔF_k, as it will be until the end. The value of δf_π is always negligible with respect to horizontal kinetic energy and pressure work divergences. A small imbalance between the four terms shown converts to A, which is important in Eq. (8.2).

We considered the possibility that the strength of the F contribution around day 5523 might have been due to the reinitialization of the model on day 5520. We initialized the model on day 5506 and integrated until Julian day 5534 to eliminate the reinitialization adjustment of the fields. This 28-day forecast experiment (shown in Pinardi and Robinson, 1986) does not differ visually from the two 14-day forecasts. The expanding phase still showed the increase of filtering activity.

Figure 13 shows that the available gravitational energy in the northwest eddy strengthens during and after the merging process due to a net positive buoyancy work. The value of A is always important in the balance of (8.2). During the latter part of the expansion phase and the relaxation phase the buoyancy work develops

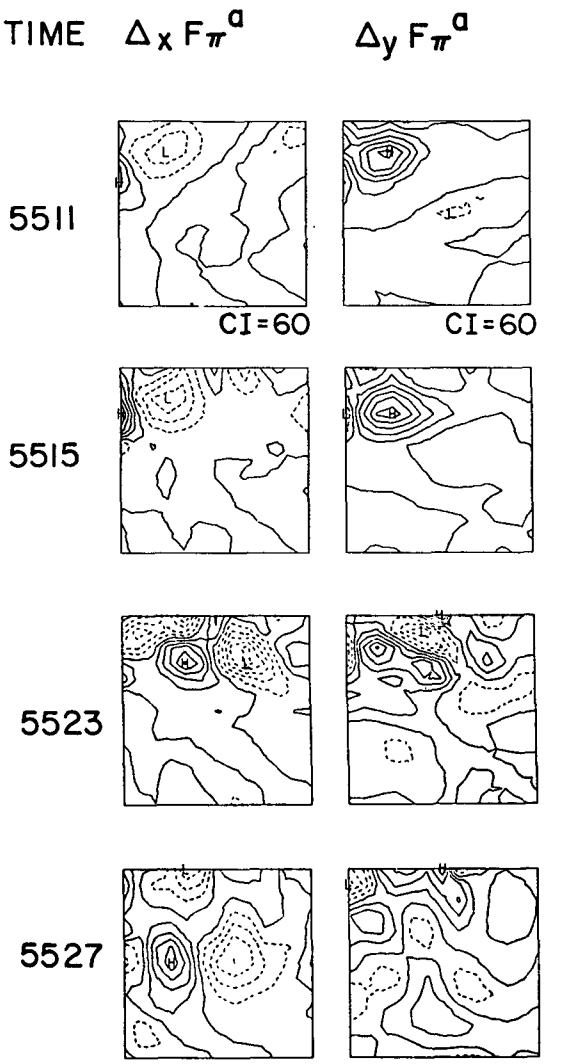

FIG. 11. Zonal and meridional components of the ΔF_π^a terms in the kinetic energy equation (8.1) computed from the forecast experiments at level 2.

a more wavelike pattern and finally weakens. The ΔF_A term becomes comparable to the buoyancy work during the expanding phase, and during the third phase it increases in scale to partially balance the buoyancy term.

In summary, the kinetic energy terms are dominated by ΔF_k, ΔF_π^a, so that the process of energy distribution and conversion in the field is connected with horizontal nonlinear transfers of energy. During the merging phase ΔF_π^a is the term that produces convergence of energy fluxes. The term ΔF_k plays a crucial role only in the expansion and relaxation phases; this term contains the divergence of momentum Reynolds fluxes, which are responsible for barotropic instability processes. The horizontal nonlinear kinetic energy transfer is followed by a net conversion of K to A. The A equation balance

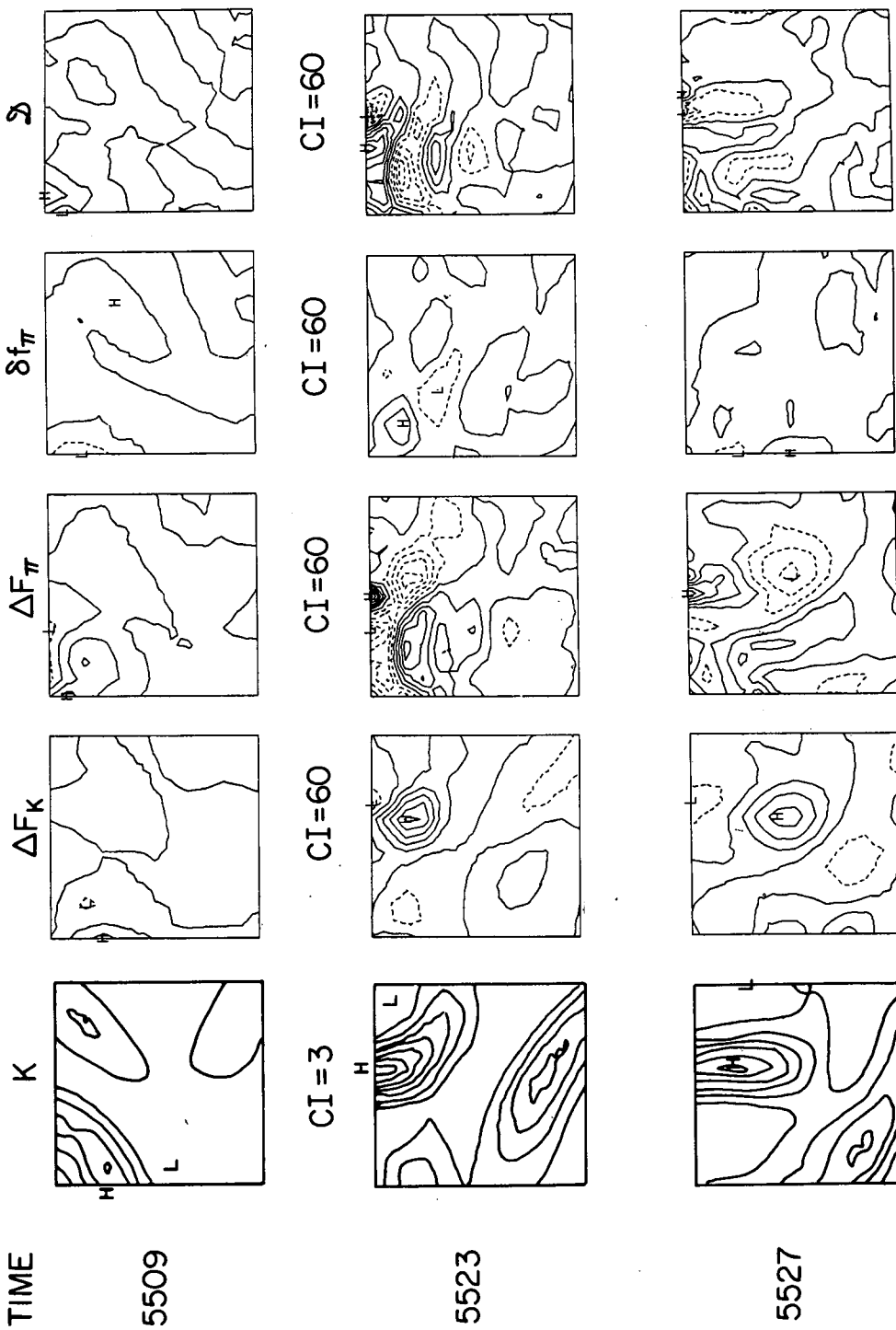

FIG. 12. As in Fig. 10 but for the kinetic energy equation (8.1).

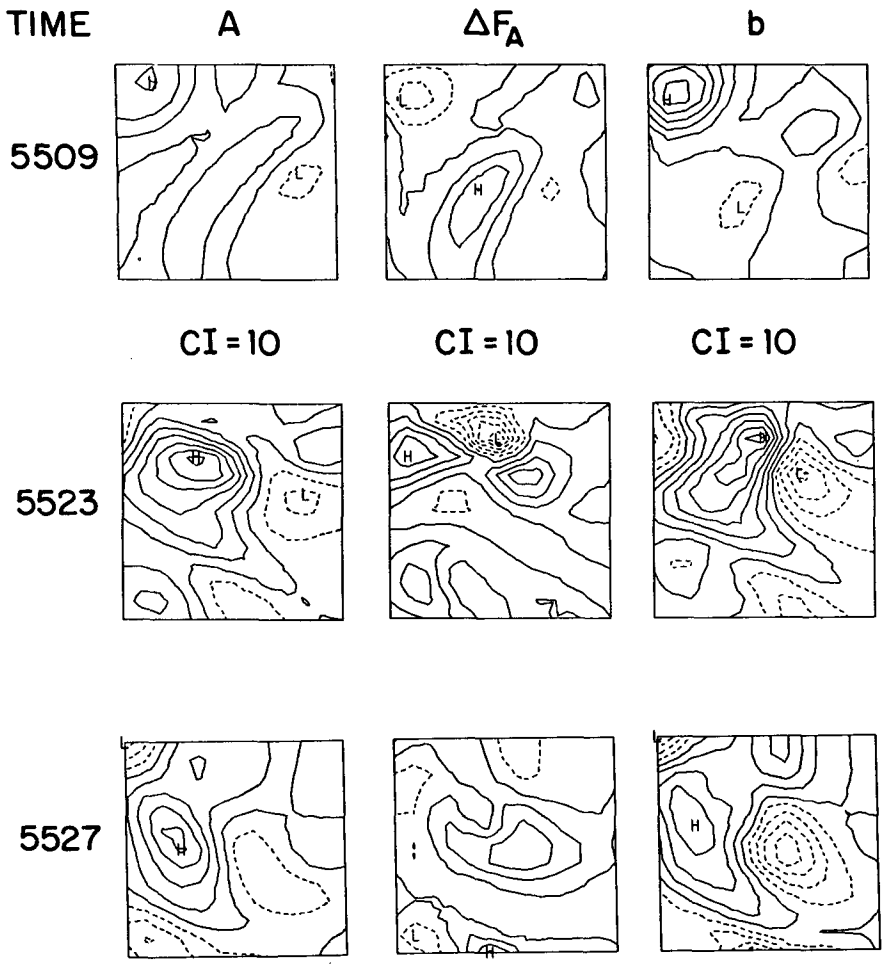

FIG. 13. As in Fig. 10 but for the available gravitational energy equation (8.2).

shows A growing from the b conversion and the ΔF_A term redistributing the energy within the region.

We believe that these results are consistent with a process of finite amplitude barotropic instability in the baroclinic fluid. The horizontal shear at the border of the two interacting eddies is decreased by the horizontal transfer mechanism due to $\Delta F_\pi{}^a$ terms, and kinetic energy is transferred by ΔF_k processes to larger horizontal scales, which have different vertical structure. Although this is a local event, it is probably related to two-dimensional turbulence cascade mechanisms.

c. Energy and vorticity diagrams

In an open domain it is important (Pinardi and Robinson, 1986) to evaluate averaged net vorticity and energy flux divergences for long enough to have meaningful energy and vorticity transport/conversion tendencies, if the ocean is statistically homogeneous in some sense. In an "eventful" ocean, long enough time series are required to define events and set them in their background context.

In Fig. 14, energy and vorticity time series of horizontally integrated terms in (7.1), (8.1) and (8.2) are displayed. The domain chosen, as indicated, is the contact point of the merger of the two original eddies. The three phases of the internal dynamical processes are evident in Figs. 14a, b and c.

The initial 1–3 day gradients are associated with dynamical adjustment of the data and are not interesting here. In the merger phase, the most noticeable change is the increase and vanishing of the spatial average $\langle \Delta F_T \rangle$, which was initially negative. Throughout all phases, $\langle \Delta F_R \rangle$ increases slowly, contributing least during the expansion phase and changing sign during relaxation. The onset of the expansion phase is shown dramatically in the $\dot{K}$ balance by the increase of ΔF_K, and the sign change and decrease of ΔF_π. Towards the end of the relaxation phase all contributions to $\dot{K}$ are diminishing in absolute value. The end of the merger phase occurs latest in the $\dot{A}$ balance of this region. Maximum rates occur during the expansion phase. The relaxation phase shows a sign change of the conversion

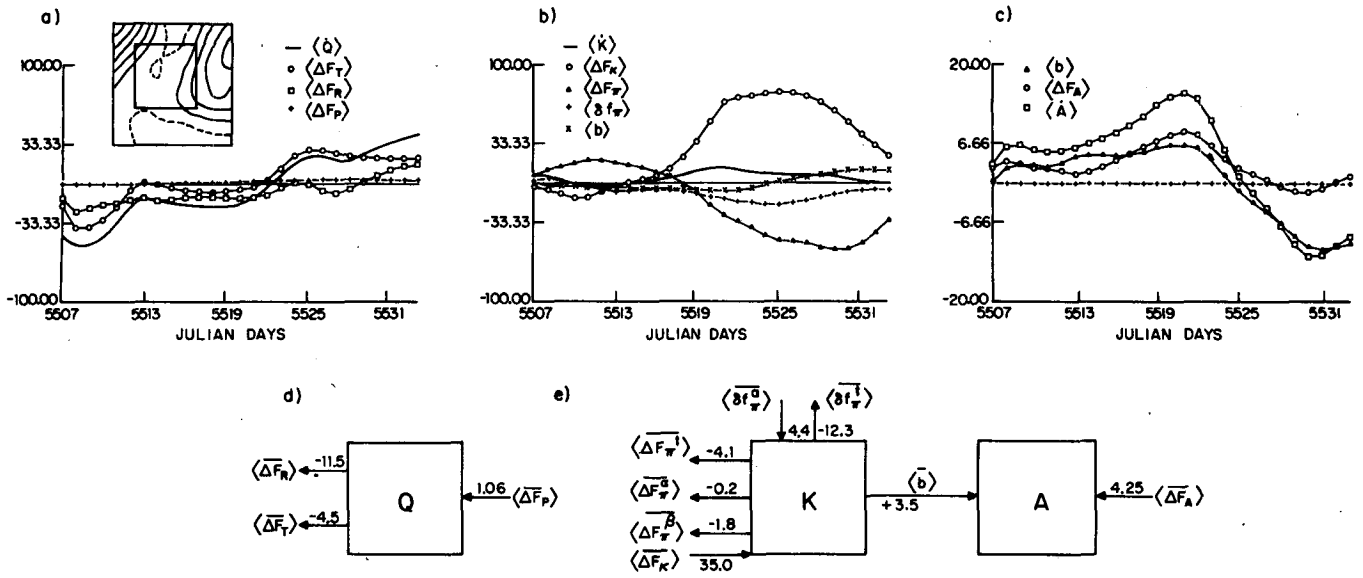

FIG. 14. Time series of terms in the vorticity and energy equations for a one-month forecast experiment beginning at 5506 and their time integral balances. Angle brackets denote space average and an overbar time average. The inner domain used for averaging is shown in the upper left. (a) Time rate of change of Q and divergences of the vorticity fluxes; (b) time rate of change of K, divergences of the kinetic energy fluxes and the negative of the buoyancy work; (c) time rate of change, advective fluxes of (a) and buoyancy work; (d), (e) vorticity and energy diagrams. Arrows show the direction of the fluxes.

$\langle b \rangle$, but we do not regard this as physically significant because of the mapped distribution (Fig. 13).

Figures 14d and 14e show for the same subregion the time- and space-integrated vorticity and energy tendencies for the first 21 days of model integration, i.e., during the merging and expanding phases. Both $\langle \overline{\Delta F_R} \rangle$ and $\langle \overline{\Delta F_T} \rangle$ are negative, indicating a net decrease of Q in that region. All the pressure work divergences transport energy away from the region, while $\langle \overline{\Delta F_k} \rangle$ transports energy into it. The energy also diverges due to the vertical pressure work divergence $\langle \overline{\delta f_\pi} \rangle$ and to the buoyancy work $\langle \bar{b} \rangle$. Also $\langle \overline{\Delta F_A} \rangle$ acts to increase A, approximately at the same rate as $\langle \bar{b} \rangle$.

The energy diagrams are representative of the time–space averaged balances in the merger region of the two eddies. We have also taken the average over the whole domain represented in Fig. 10, and the only qualitative change is that the $\langle \bar{b} \rangle$ term contributes more than $\langle \Delta F_A \rangle$ to the increase of A during the merger and expansion phases. The energy diagram confirms the interpretation that the process of merging and expansion is due to a horizontal redistribution of kinetic energy, which enhances a conversion of K to A. The sign of the $\langle \Delta F_k \rangle$ and $\langle \Delta F_\pi{}^a \rangle$ is consistent with barotropic instability processes as shown in Pinardi and Robinson (1986).

9. Conclusions

We have described the evolution and kinematics of the vigorous, variable mesoscale currents in the eddy and jet regime of the California Current System. The study was carried out in a relatively flat, deep sea region (150 km)^2 for a period of four weeks. Observations combined by objective analysis but primarily by dynamical interpolation provided a synoptic time series summarized in section 5. There is a merger of two eddies, which forms a zonal jet, followed by an expansion of the surviving eddy, whose edge is connected to the intensified and meandering jet. Finally, the system relaxes to a single large, less energetic eddy.

The experiment was conducted in order (i) to attempt for the first time a real-time dynamical forecast of the oceanic synoptic/mesoscale currents; (ii) to contribute to the methodology of nowcasting, forecasting and data assimilation (optimal field estimation); (iii) to investigate the local internal dynamical processes governing the physics of this complex region; and (iv) to contribute to the development of general methods of obtaining dynamical information from direct measurements of the physical fields in an open ocean region. These objectives, of course, overlap considerably. The ability to forecast depends on the relative importance of dynamical processes and events occurring within the regime to the propagation of features through the region, etc. In turn, the ability to deduce physical processes depends upon the accuracy of field estimates, which are essentially identical to the nowcast and forecast fields.

The forecasts carried out in real time produced generally good results, except for the edges, even in our small domain. This is because of the intense internal dynamical events governing the flow evolution. Forecast experiments (hindcasts) that used boundary conditions linearly interpolated to future observations gave very good results. The interior field measurements for legs 2 and even 3 are really not necessary in order to

describe the major features of the evolution of the flow. They could have been replaced by two AXBT flights only around the perimeter of the domain. Moreover there are trade-offs. If the internal events had not been so vigorous, we would have been able to construct and utilize a time-dependent correlation function and to forecast statistically the boundary condition for the dynamical forecast (as we do in the POLYMODE region). The prospects for maintaining efficiently updated field estimates of given accuracy are excellent.

These results contribute to the verification of the quasi-geostrophic model and indicate its applicability for data assimilation and optimal field estimation and for local dynamical process studies. Indeed, the dynamical interpolation method involving the initialization of a dynamical model with real data was essential in our study to obtain unambiguously connected descriptions of fields obtained quasi-synoptically only two weeks apart. Dynamical interpolation is emerging as a powerful tool of modern synoptic, descriptive oceanography. Confining our experiment to a small domain and only using hydrographic data was, of course, only a matter of available resources and convenient logistics. Most aspects of the methodology are immediately generalizable to larger domains and to the combination of data from multiple sensors and sampling schemes, including remote sensors. We conceived of this experiment (OPTOMA-V) as a prototype dynamical forecasting exercise and regard it in this sense as a successful proof of concept. We are presently analyzing results from a subsequent experiment of two months duration carried out in an extended region a year later (OPTOMA-XI).

The synoptic time series obtained from our (OPTOMA-V) intensive dataset provides a unique example of the merger of two oceanic mesoscale eddies. The dynamics of this event and its subsequent evolution are of some general interest in geophysical fluid dynamics, as well as to the physical explanation of the California Current System variability. We analyzed the energy and vorticity dynamics of the region using an open-ocean quasi-geostrophic scheme, EVA. The results are summarized in the last paragraph of section 8a and the last two paragraphs of section 8b. Horizontal nonlinear scale interactions characteristic of finite amplitude barotropic instability and two-dimensional turbulence occur, which are modified by three-dimensional baroclinic processes including vortex stretching and the vertical transfer of energy by pressure-work flux. The merger and expansion events convert kinetic to available gravitational energy in the region.

We are continuing our research on the local dynamics of the California Current System and on the methodology of real-time forecasting and data assimilation. For the OPTOMA experiments subsequent to those reported here we devised a method of dynamical model initialization that replaces the complexity of the star-shaped ship track by a simple square module; dynamical interpolation provides adequate vorticity estimates.

Acknowledgments. We are grateful to our colleagues Dr. Everett F. Carter, Mr. Wayne G. Leslie, Dr. Michele M. Rienecker, Dr. Jerome A. Smith and Mr. Leonard J. Walstad for their contributions to data acquisition, transmission, real-time analysis, and forecasting. The skill and cooperation of Captain Steve Bliss and the crew of R.V. *Acania* were invaluable to the success of our experiments. It is a pleasure to thank the Office of Naval Research for their support via contracts to Harvard University (N00014-84-0461) and the Naval Postgraduate School (N00014-84-NR24501).

REFERENCES

Carter, E. F., and A. R. Robinson, 1986: Analysis models for the estimation of oceanic fields. *J. Atmos. Oceanic Technol.*, **3**(4), (in press).

Heath, G. R., 1983: Oceanographic studies through December 1982 at Pacific study area W–N, Low Level Waste Ocean Disposal Program. Rep. OSU-19, Oregon State University, 173 pp.

Miller, R. N., A. R. Robinson and D. B. Haidvogel, 1983: A baroclinic quasi-geostrophic open ocean model. *J. Comput. Phys.*, **50**, 38–70.

Mooers, C. N. K., and A. R. Robinson, 1984: Turbulent jets and eddies in the California current and inferred cross-shore transports. *Science*, **223**, 51–53.

Pinardi, N., and A. R. Robinson, 1986: Local quasi-geostrophic energetics of open ocean regions. *Journal*, (in press).

Rienecker, M. M., C. N. K. Mooers, D. E. Hagan and A. R. Robinson, 1985: A cool anomaly off northern California: An investigation using IR imagery and *in situ* data. *J. Geophys. Res.*, **90**, 4807–4818.

Robinson, A. R., and W. G. Leslie, 1985: Estimation and prediction of oceanic eddy fields. *Progress in Oceanography*, vol. 14, Pergamon, 485–510.

——, J. A. Carton, C. N. K. Mooers, E. F. Carter, M. M. Rienecker, J. A. Smith and W. G. Leslie, 1984: A real-time dynamical forecast of ocean synoptic/mesoscale eddies. *Nature* **309**, 781–783.

Smith, J. A., C. N. K. Mooers and A. R. Robinson, 1985: Estimation of baroclinic quasi-geostrophic modal amplitudes from XBT/CDT survey data. *J. Atmos. Oceanic Technol.*, **2**, 491–507.

Wittman, P. A., M. M. Rienecker, E. A. Kelley and C. N. K. Mooers, 1985: Hydrographic data from the OPTOMA program: OPTOMA 5. NPS 68-85-003, Naval Postgraduate School, 97 pp.

Wyllie, J. G., 1966: Geostrophic flow of the California current at the surface and at 200 m. *Atlas of the California Cooperative Oceanic Fisheries Investigation*, No. 4, 13 pp., 288 charts.